



# Searching for the 3.5 keV Line in the Deep Fields with *Chandra*: The 10 Ms Observations

Nico Cappelluti<sup>1,2,3</sup>, Esra Bulbul<sup>4,5</sup>, Adam Foster<sup>5</sup>, Priyamvada Natarajan<sup>6</sup>, Megan C. Urry<sup>1</sup>,Mark W. Bautz<sup>4</sup>, Francesca Civano<sup>5</sup>, Eric Miller<sup>4</sup>, and Randall K. Smith<sup>5</sup><sup>1</sup>Yale Center for Astronomy and Astrophysics, P.O. Box 208121, New Haven, CT 06520, USA<sup>2</sup>Department of Physics, Yale University, P.O. Box 208121, New Haven, CT 06520, USA<sup>3</sup>Physics Department, University of Miami, Coral Gables, FL 33124, USA<sup>4</sup>Kavli Institute for Astrophysics & Space Research, Massachusetts Institute of Technology, 77 Massachusetts Avenue, Cambridge, MA 02139, USA<sup>5</sup>Harvard-Smithsonian Center for Astrophysics, 60 Garden Street, Cambridge, MA 02138, USA<sup>6</sup>Department of Astronomy, Yale University, P.O. Box 208101, New Haven, CT 06520, USA

Received 2017 January 25; revised 2018 January 9; accepted 2018 January 16; published 2018 February 26

## Abstract

We report a systematic search for an emission line around 3.5 keV in the spectrum of the cosmic X-ray background using a total of  $\sim 10$  Ms *Chandra* observations toward the COSMOS Legacy and Extended *Chandra* Deep Field South survey fields. We find marginal evidence of a feature at an energy of  $\sim 3.51$  keV with a significance of  $2.5\text{--}3\sigma$ , depending on the choice of statistical treatment. The line intensity is best fit at  $(8.8 \pm 2.9) \times 10^{-7} \text{ ph cm}^{-2} \text{ s}^{-1}$  when using a simple  $\Delta\chi^2$  or  $10.2^{+0.2}_{-0.4} \times 10^{-7} \text{ ph cm}^{-2} \text{ s}^{-1}$  when Markov chain Monte Carlo is used. Based on our knowledge of *Chandra* and the reported detection of the line by other instruments, an instrumental origin for the line remains unlikely. We cannot, however, rule out a statistical fluctuation, and in that case our results provide a  $3\sigma$  upper limit at  $1.85 \times 10^{-6} \text{ ph cm}^{-2} \text{ s}^{-1}$ . We discuss the interpretation of this observed line in terms of the iron line background, S XVI charge exchange, as well as potentially being from sterile neutrino decay. We note that our detection is consistent with previous measurements of this line toward the Galactic center and can be modeled as the result of sterile neutrino decay from the Milky Way for the dark matter distribution modeled as a Navarro–Frenk–White profile. For this case, we estimate a mass  $m_\nu \sim 7.01$  keV and a mixing angle  $\sin^2(2\theta) = (0.83\text{--}2.75) \times 10^{-10}$ . These derived values are in agreement with independent estimates from galaxy clusters, the Galactic center, and M31.

**Key words:** astroparticle physics – dark matter – diffuse radiation – Galaxy: halo – X-rays: diffuse background

## 1. Introduction

Astrophysical and cosmological observations of gravitational interactions of visible baryonic matter provide overwhelming evidence for the existence of an additional dominant component of nonluminous matter, referred to as dark matter (see, e.g., Rubin & Ford 1970). Extensive direct and indirect searches for this ubiquitous matter have so far failed to detect it, and its nature remains unknown. The majority of this unseen component is inferred to be cold and collisionless, but a warmer component can also be accommodated to account at least partially for the overall mass budget of dark matter. X-ray observations of dark-matter-dominated objects, such as galaxies and clusters of galaxies, provide a unique laboratory for searching for the decay or annihilation of a viable warm dark matter candidate, namely sterile neutrinos (Dodelson & Widrow 1994; Abazajian et al. 2001; Dolgov & Hansen 2002; Boyarsky et al. 2006).

An unidentified emission line near 3.5 keV was recently detected in stacked observations of galaxy clusters and in the Andromeda galaxy (Boyarsky et al. 2014; Bulbul et al. 2014, *Bo14* and *Bul14a* hereafter). The interpretation of this signal as arising from decaying dark matter has drawn considerable attention from the astrophysics and particle physics communities. The line is also detected in the *Suzaku* and *NuSTAR* observations of the core of the Perseus and Bullet clusters (Wik et al. 2014; Urban et al. 2015; Franse et al. 2016) and in the Galactic center (Boyarsky et al. 2015). An emission line at a consistent energy is also detected in *XMM-Newton* observations of the Galactic center and in other individual clusters (Iakubovskiy et al. 2015). Recently, an  $11\sigma$  detection of the line was reported in summed *NuSTAR* observations of the

COSMOS and Extended *Chandra* Deep Field South (CDFs) survey fields, where a dark matter signal from the Milky Way halo may be expected (Neronov et al. 2016). As noted, another interesting dark matter candidate that might also produce a 3.5 keV X-ray line is self-interacting dark matter from relatively low mass, axion-like particles (e.g., Conlon & Day 2014).

Although the line was detected by several X-ray satellites, including *XMM-Newton*, *Chandra*, *Suzaku*, and *NuSTAR* in a variety of dark-matter-dominated objects, several other studies report nondetections of the line, such as in stacked *Suzaku* observations of clusters of galaxies (Bulbul et al. 2016), in the dwarf galaxy Draco (Ruchayskiy et al. 2016), and in *Hitomi* observations of the Perseus cluster (Hitomi Collaboration et al. 2017). However, the upper limits derived from the stacked galaxies are in tension with the original detection at the  $5\sigma$  level (Anderson et al. 2015).

Despite these intensive and persistent efforts, the origin of the 3.5 keV line remains unclear. Potential astrophysical interpretations were discussed extensively by Bul14a. A more recent update is provided by Franse et al. (2016), who consider an additional model that comprises a charge exchange between bare sulfur ions and neutral gas (e.g., Bul14a; Gu et al. 2015; Shah et al. 2016). The radial distribution of the flux of the line can provide an independent test of its origin; however, the observed line flux from the Perseus core is consistent with a dark matter origin (Franse et al. 2016). However, the intensity of the signal in the cluster core appears to be anomalously high for the decaying dark matter model (Bul14a; Franse et al. 2016). In their recent paper, the *Hitomi* collaboration measured the K XVIII abundance for the first time as  $0.6Z_\odot$ , well within the allowed limits in Bul14a in the core of the Perseus cluster

(Hitomi Collaboration et al. 2017). The other possible astrophysical line that was suggested as a contaminant is Ar XVII DR from lab studies of electron beam ion trapping measurements (E. Bulbul et al. 2017, in preparation). These results have eliminated the K XVIII and Ar XVII DR lines as the possible origin for the 3.5 keV line. The *Hitomi* collaboration reports tension between the flux in the Perseus cluster observed by *XMM-Newton* and *Hitomi* at the  $3\sigma$  level. The authors attribute this discrepancy to subtle instrumental features in earlier observations of *Hitomi*.

Here, we report the detection of the line at  $\sim 3.5$  keV in the summed data from deep *Chandra* blank fields, CDFS, and COSMOS for a total exposure of 9.17 Ms. We critically discuss instrumental effects together with four plausible explanations for the origin of the 3.5 keV line: charge exchange, the iron line background, a statistical fluctuation, and dark matter decay. All errors quoted throughout the paper correspond to 68% single-parameter confidence intervals. Throughout our analysis, we use a standard  $\Lambda$ CDM cosmology, adopting the following values for the relevant parameters:  $H_0 = 71 \text{ km s}^{-1} \text{ Mpc}^{-1}$ ,  $\Omega_M = 0.27$ , and  $\Omega_\Lambda = 0.73$ .

## 2. Data Sets

The *Chandra*-COSMOS Legacy Survey (CCLS; Scoville et al. 2007; Elvis et al. 2009; Civano et al. 2016) and the CDFS (Giacconi et al. 2002; Luo et al. 2008; Xue et al. 2011; B. Luo 2016, in preparation) have been observed for  $\sim 4.6$  M and  $\sim 7$  Ms, respectively, with the ACIS-I CCD instrument on board *Chandra* with 117 and 111 pointings, respectively. The CCLS field is a relatively shallow mosaic of  $\sim 2 \text{ deg}^2$  with an average exposure of  $\sim 160 \text{ ks pix}^{-1}$ , whereas the CDFS field is a deep pencil beam survey of  $\sim 0.1 \text{ deg}^2$  observed for  $7 \text{ Ms pix}^{-1}$ . However, since the signal is very faint, for spectral analysis we have only used the pointings observed in the VFaint telemetry mode with a focal plane temperature of 153.5 K, in order to minimize the instrumental background. Since the CDFS was partly observed in the early phase of the mission when the VFaint mode was not available and observations were partly taken at higher temperature, the total exposure time before treatment is  $\sim 6$  Ms.

## 3. Data Analysis

Raw event files were calibrated using the CIAO tool *chandra\_repro* and the Calibration Database (CALDB) version 4.8. For every pointing, time intervals with high background were cleaned using the CIAO tool *deflare* using the *lc\_clean* technique as described by Hickox & Markevitch (2006). The deflaring was performed in the [2.3–7] keV, [9.5–12] keV, and [0.3–3] keV energy bands in sequence, in order to detect flares with anomalous hardness ratios (Hickox & Markevitch 2006). Although not critical for this work, the astrometry was aligned using reference optical catalogs.

The X-ray signal is a blend of detected and unresolved active galactic nuclei (AGNs), galaxies, and clusters whose summed emission is often referred to as the cosmic X-ray background (CXB). There is also a particle-induced background and a (relatively small) background from other sources within the instrument. Hereafter we will use the acronym CXB for the signal produced by all astrophysical sources that is focused by the optics, and we adopt the acronym PIB for the particle and

**Table 1**  
[2.4–7] keV Net Counts and Exposures

	Signal (counts)	Background (counts)	Exposure (Ms)
CDFS	115373	1989189	5.57
CCLS	131826	1220611	3.59
Total	247199	3209800	9.16

instrumental background that is produced by all other (nonastrophysical) sources.

For the sake of clarity, in this paper, the putative 3.5 keV signal arising either from dark matter decay or sulfur charge exchange will be considered as a separate component on top of the CXB and PIB signal. Therefore, we start the analysis by carefully accounting for known X-ray sources that constitute the PIB and the CXB.

### 3.1. Extraction of Summed X-Ray Spectrum

The detected intensity of the CXB is not the same across the surveys presented here, primarily due to cosmic variance, so we derive an independent spectrum for each survey field. For each pointing, we extracted the spectrum of all the photons detected in the ACIS-I field of view (FOV) with the CIAO tool *specextract*. For each spectrum, we then computed the field-averaged redistribution matrix functions and ancillary response functions (ARF) using the CIAO tool *specextract*. Spectra were coadded and response matrices averaged after weighting by the exposure time. We produced a cumulative CXB+PIB spectrum for each of the data sets. Because we are looking for diffuse emission, the only background component in our observations is the PIB. The *Chandra X-ray Observatory* periodically obtains “dark frames,” that is, exposures with ACIS in the stowed mode. When the High Resolution Camera is on the focal plane, ACIS is stowed and unexposed to any focused source, but it still records the PIB component. In such a position, the ACIS detectors see neither the sky nor the calibration sources. In particular, Hickox & Markevitch (2006) demonstrated that the [2–7] keV to [9.5–12] keV hardness ratio is constant (within 2%) in time regardless of the amplitude of the particle background. Therefore, we employed ACIS-I observations in the stowed mode to evaluate the background. In particular, we merged the *stowed* mode event files, applied the VFaint filtering, and reprojected to the same astrometric frame as the observations. We then extracted the spectrum in the same source-masked regions and renormalized it by the ratio of count rates in energy bins  $C_{[9.5-12],\text{obs}}/C_{[9.5-12],\text{stow}}$ , where  $C_{[9.5-12],\text{obs}}$  and  $C_{[9.5-12],\text{stow}}$  are the number of photons in the stow and real data, respectively. In a recent paper, Bartalucci et al. (2014) performed a detailed and sophisticated analysis of the same stowed ACIS-I event files employed here and reported, to within 2%, the relative stability of the background in observations of later epochs compared to those used by Hickox & Markevitch (2006). In this paper, we are looking methodically for astrophysical emission lines in the energy range [2.4–7] keV. In this energy band, the PIB is affected by a systematic uncertainty of the order of 2%, which is added in quadrature to the PIB spectral data error bars throughout our analysis. In Table 1, we summarize the number of net counts used for the spectral modeling and the resulting vignetting-weighted final exposures for our data sets. However, we note that the observations in the stowed mode are much

shorter than those employed here (a total of 1 Ms in the archive versus 9.16 Ms). This, of course, significantly limits our sensitivity, since the PIB spectrum has larger errors than those in the data and therefore might potentially artificially smooth out any features in the data.

### 3.2. About the Spectrum of PIB

Part of the signal included in the total X-ray spectrum is due to the PIB. In order to find faint sources or to analyze faint, diffuse emission lines, careful treatment of these backgrounds is essential. We start by examining data from ACIS-I in stowed mode, that is, when no cosmic photons are collected. This provides a robust representation of the particle background plus internal instrumental background. Although a universal model of the PIB is not provided by the *Chandra* team, here we can model the PIB using a broken power law, with the slopes ( $\Gamma_{\text{PIB},1}$ ,  $\Gamma_{\text{PIB},2}$ ), the break energy ( $E_{\text{break}}$ ), and the normalization (*norm*) as free parameters. On top of this, we add a Gaussian model at  $E \sim 2.5$  keV and  $E \sim 5.9$  keV, with energies and intensities ( $I_{1,2}$ ) that are free to vary. The line at 5.9 keV is a known Mn  $K_{\alpha}$  instrumental feature. This feature is scattered light from the radioactive  $^{55}\text{Fe}$  in the external calibration source. This source has a half-life of  $\sim 2.7$  years, so its intensity has dropped dramatically over the course of the *Chandra* mission. So it is not surprising that it (and its K escape and Ti line) is not fully subtracted from the CXB spectrum. The line at 2.51 keV is instrumental and an artifact: Bartalucci et al. (2014) pointed out that in the [2–3] keV energy band, due to the position-dependent charge transfer inefficiency (CTI) correction, the strong, broad emission line at  $\sim 2.1$  keV (mother line) produces a system of spurious daughter lines at energies of up to  $\sim 2.6$  keV along with spurious broadening. A similar effect is observed above 7.3 keV as well. CTI correction is necessary because radiation has damaged the ACIS-I, resulting in loss in the CTI. This damage, however, did not affect areas of the CCD not exposed to the X-rays, such as the frame store area. To cope with the CTI, a correction is applied a posteriori by the data analysis pipeline. This correction is applied to all of the data, including those collected by areas not damaged by radiation. The result is that for the strongest instrumental emission lines, the recorded energy is artificially shifted up to 800 eV higher energy (depending on the position on the detector). Detailed modeling of PIB is beyond the scope of this paper, and we refer the readers to the *Chandra* Calibration Database and to specific papers (see, e.g., Bartalucci et al. 2014).

## 4. Results

As noted in Table 1, the spectra analyzed in this paper are background dominated, and this might raise concern when looking for faint emission lines. In this section, we present two different approaches to presenting the results based on two independent methods to handle the background. In the first, we subtract the properly normalized PIB spectra from the data and fit, and in the second, we fit the CXB+PIB at the same time with models for each component. If we detected the 3.5 keV line and if it is diffuse coming from the entire field of view, we performed the fit using data accumulated over the whole detector and after masking the detected sources.

### 4.1. Fitting the Background-subtracted Full Spectra Including Point Sources

XSPEC v12.9.0 was used to perform the spectral fits with  $\chi^2$  as an estimator of the goodness of fit. The spectral counts in each energy bin are sufficient to allow the use of Gaussian statistics in this analysis (Protassov et al. 2002). To increase the sensitivity to weak emission lines, we simultaneously fit the CXB spectra from the CCLS and CDFS. We restrict the energy range to 2.4–7 keV in order to avoid the bright *Au* feature at 2 keV, while having sufficient leverage on the power-law component. The Galactic column densities are fixed to  $2.5 \times 10^{20} \text{ cm}^{-2}$  for the fits of the CCLS field and  $8.8 \times 10^{19} \text{ cm}^{-2}$  for the CDFS field (Dickey & Lockman 1990). The power-law indices and the normalizations are left free in our fits to account for the different CXB fluxes in the two fields (Hickox & Markevitch 2006). We first fit the spectra with a single absorbed (*wabs* model in XSPEC) power-law model that gives an overall good fit with  $\chi^2$  of 563.43 for 308 degrees of freedom (dof). The best-fit power-law normalizations are found to be  $\sim 2.78 \times 10^{-4} \text{ ph keV}^{-1} \text{ cm}^{-2} \text{ s}^{-1}$  in CDFS and  $2.80 \times 10^{-4} \text{ ph keV}^{-1} \text{ cm}^{-2} \text{ s}^{-1}$  in CCLS. The power-law indices are  $\Gamma_1 = 1.82 \pm 0.10$  and  $\Gamma_2 = 1.48 \pm 0.06$  for the two fields, respectively (hereafter the subscripts 1 and 2 will refer to CDFS and CCLS, respectively). The fluxes and spectral indices measured here are in agreement with Hickox & Markevitch (2006), Moretti et al. (2012), Bartalucci et al. (2014), and Cappelluti et al. (2017a).

A few spectral features are immediately visible around 2.51, 3.15, 3.5, 4.4, and 6.4 keV. The 2.51 keV line is a strong *Au*-M complex line. We tried to fit the feature at 3.15 keV and did not find a significant line but only found a  $3\sigma$  upper limit of  $\sim 1.5 \times 10^{-6} \text{ ph keV}^{-1} \text{ cm}^{-2} \text{ s}^{-1}$ ; this means that the feature is just a statistical fluctuation in a few channels. The emission line at 4.37 keV is consistent with a residual from a blend of known instrumental emission lines from silicon escape (i.e., lines formed by electron clouds left when a photon carrying away energy leaves a silicon substrate)<sup>7</sup> from Mn  $K_{\alpha,1,2}$  and Ti  $K_{\alpha,1,2}$  given<sup>8</sup> that the energy resolution is  $>200$  eV at these energies. These two weak emission lines are hard to detect in the PIB due to limited statistics, but they become clearly visible in the deep blank-sky observations used here or can be produced by a minimal leaking of the on-board calibration source. The line at 6.4 keV is consistent with Fe  $K_{\alpha}$ , and for this line we cannot discriminate between an instrumental or a Galactic origin. Adding the Gaussian components for the instrumental lines at 2.51, 3.15, 4.4, and 6.4 keV with variable energies and normalizations improves the  $\chi^2$  value by a significant amount with  $\chi^2$  of 527.01 for 298 dof.

We present the data and the best-fit model obtained with (right panel) and without (left panel) a Gaussian line added in the model at the 3.5 keV line in Figure 1. The best-fit energy of the Gaussian at the 3.5 keV line becomes  $3.51_{-0.02}^{+0.02} \text{ keV}$  with a flux of  $(8.83 \pm 2.9) \times 10^{-7} \text{ ph cm}^2 \text{ s}^{-1}$ . If this line is removed from the fit, the change in  $\chi^2$  value becomes 536.93 ( $\Delta\chi^2$  of 10.23) for 2 dof, corresponding to a detection confidence level of  $3.2\sigma$ . From the  $\chi^2$  contour, we determine a  $3\sigma$  upper limit of  $1.75 \times 10^{-6} \text{ ph cm}^2 \text{ s}^{-1}$ . This would correspond to  $P \sim 0.003$  (i.e., probability that the line is not present). However, in cases like this, the model is not correctly specified (the best fit should

<sup>7</sup> [http://cxc.harvard.edu/cal/Acis/Cal\\_prods/matrix/notes/Fl-esc.html](http://cxc.harvard.edu/cal/Acis/Cal_prods/matrix/notes/Fl-esc.html)

<sup>8</sup> [http://www.astro.wisc.edu/~bessemer/images/REU\\_Poster\\_port.pdf](http://www.astro.wisc.edu/~bessemer/images/REU_Poster_port.pdf)



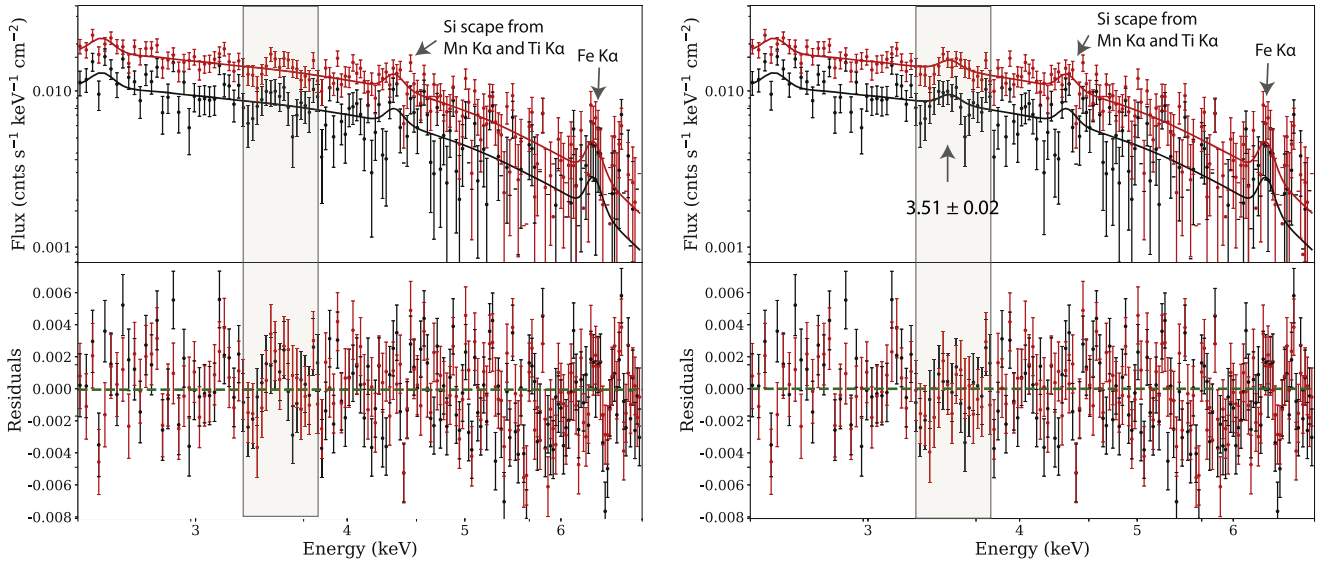


**Figure 1.** Left panel: CXB spectra in the CDFS (in black) and CCLS (red) together with best-fit models (solid lines) and the residuals without the 3.5 keV line Gaussian model component. Right panel: the same by adding a Gaussian model at  $\sim 3.5$  keV. The known instrumental lines of Si escape peak from Mn K $\alpha$ , Ti K $\alpha$  at 4.4 keV, and Fe K $\alpha$  at 6.4 keV are marked in both panels.

have had  $\chi^2 \sim 298$ ): when the model is misspecified, the traditional correspondence between  $\Delta\chi^2$  and  $P$  breaks down (see, e.g., Spanos 2010). To fully understand the actual level of  $P$ , one would need to perform more detailed tests that, because of the statistics, we did not perform in this work. However, we tested if the addition of the emission lines improved the quality of fit with the Bayes and Akaike information criteria (Schwarz 1978; BIC and AIC, respectively). The change in BIC value is  $\sim 15$ , while the AIC suggests that the power-only fit is  $\sim 10^6$  times less likely than the power law plus emission lines model. However, when the BIC is computed between the power-law model and the power law plus any single detected emission line, the quality of the fits is marginally improved. This is indeed one of the limitations of BIC, which tends to discard more complicated models and is not sensitive to low signal-to-noise ratio signals. The AIC instead always favors the power law plus emission lines. We also use the Markov chain Monte Carlo (MCMC) solver in XSPEC to determine the full probability distribution of the free fit parameters including the instrumental lines. Using the Metropolis–Hastings algorithm, we run five chains, each with a length of 25,000, and we discard the first 5000 steps in each run for the burn-in period. Integrating over all of the parameters, we obtain the posterior distribution for each variable parameter ( $P(X)$ ). Figure 2 shows the derived  $P(X)$  for each parameter (excluding instrumental lines) and the confidence contours and the best-fit parameters. The best-fit power-law continuum parameters are  $\Gamma_1 = 1.89^{+0.10}_{-0.11}$ ,  $\Gamma_2 = 1.50^{+0.07}_{-0.07}$ , and fluxes  $\log(I_{\text{PL},1}) = -3.56 \pm 0.01 \text{ ph cm}^2 \text{ s}^{-1}$  and  $\log(I_{\text{PL},2}) = -3.56 \pm 0.04 \text{ ph cm}^2 \text{ s}^{-1}$ , in agreement with Hickox & Markevitch (2006) and Cappelluti et al. (2017b; see Table 3). The continuum parameter best fits are summarized in Table 3; note that, in this case, flux is accumulated on a  $16'9 \times 16'9$  area. The best-fit energy and the flux of the 3.5 keV line are consistent with those obtained with the  $\chi^2$  fit and are  $E = 3.51^{+0.03}_{-0.02} \text{ keV}$  and  $I_{3.5} = 10.2^{+0.2}_{-0.4} \times 10^{-7} \text{ ph cm}^2 \text{ s}^{-1}$ .  $P(I_{3.5})$  is very asymmetric with a tail toward low values with a floor at  $3\sigma$  at  $7.2 \times 10^{-8} \text{ ph cm}^2 \text{ s}^{-1}$ , hence confirming the significance of the line detection at  $\sim 3\sigma$  confidence. In Table 2 we report all of

**Table 2**  
Best-fit Emission Line Parameters from the Joint Fits of Deep-field CXB Spectra Obtained within the MCMC Method

Energy keV	Flux $10^{-6} \text{ ph cm}^{-2} \text{ s}^{-1}$
$2.51 \pm 0.01$	$52.80 \pm 19.64$
$3.51 \pm 0.02$	$1.02 \pm 0.41$
$4.37 \pm 0.03$	$1.12 \pm 0.29$
$6.38 \pm 0.04$	$1.98 \pm 0.55$
$\chi^2$ (dof)	527.01 (298)

**Table 3**  
Best-fit Model Continuum of the Two Fields CXB Spectra

Parameter	Value	Unit
$\Gamma_1$	$1.89^{+0.10}_{-0.11}$	...
$\Gamma_2$	$1.50^{+0.07}_{-0.07}$	...
$\log(I_{\text{PL},1})$	$-3.56 \pm 0.01$	$\text{ph cm}^2 \text{ s}^{-1}$
$\log(I_{\text{PL},2})$	$-3.56 \pm 0.04$	$\text{ph cm}^2 \text{ s}^{-1}$

the detected emission line parameters. The  $3\sigma$  upper limit found with MCMC is  $1.85 \times 10^{-6} \text{ ph cm}^2 \text{ s}^{-1}$ . However, we point out that, like in the  $\chi^2$  fit case, MCMC can only reflect statistical variations and does not treat model misspecification. This problem will be approached in a forthcoming paper that will employ a larger sample.

#### 4.2. Fitting the Background-subtracted, Source-masked Spectra

As a further test, we fit the spectrum obtained after masking all of the known point and extended sources in the field. At the time of the analysis, the latest public catalog of CDFS sources was produced with the 4 Ms exposure of Xue et al. (2011). We mosaic all of the available observations and produce exposure maps as described by Cappelluti et al. (2016). We then run CIAO’s source-detection algorithm *wavdetect* in

the [0.5–2] keV, [2–7] keV, and [0.5–7] keV energy bands. We set a threshold of  $10^{-5}$  (see CIAO detection manual), and the faintest detected sources have fluxes of the order  $10^{-17}$  erg cm $^{-2}$  s $^{-1}$ . For each point and extended source, we create regions with a spatial extent of  $5\sigma$  of the point-spread function (PSF) around the centroid (ranging from  $\sim 1''$  to  $1.5''$  FWHM at the center of the image to  $>5''$  at the outskirts). The three-band catalogs are merged, and sources in each of the bands are removed from the event files of each pointing.<sup>9</sup>

CCLS has a completely different tiling of pointings. Therefore, source detection requires a more complicated procedure. For CCLS, we employ the catalog published by Civano et al. (2016) and mask sources within  $\sim 10''$  around each detection. According to Figure 9 of Civano et al. (2016), this procedure will safely remove  $>90\%$  of the sources' flux in the energy bands investigated here. An emission line with a best-fit energy of 3.51 keV is detected at the  $2.5\sigma$  confidence level. Although less strongly than above, even in this configuration the BIC and the AIC still favor the power law plus emission lines, and the confidence contours obtained from MCMC analysis are shown in Figure 3. The best-fit energy and flux parameters found in the MCMC analysis are  $E = 3.51^{+0.04}_{-0.04}$  keV and  $I_{3.5} = 5.8^{+4.6}_{-3.8} \times 10^{-7}$  ph cm $^2$  s $^{-1}$ , respectively. The line energy is poorly constrained while the intensity has been found larger than zero  $>97\%$  of the time, therefore providing evidence for the line at around  $2.5\sigma$ .

The best-fit energy and flux found in source-included and source-excluded spectra are in agreement within the  $1\sigma$  level. The detection of the 3.5 keV line in the source-excluded fit is less stringent than the source-included case. This is because the source masking, especially in the CDFS, removes a larger fraction of the data ( $>50\%$ ), and hence the statistics on the continuum are severely affected. Therefore, the power law and the flux of the 3.51 keV line continuum are weakly constrained. Since we detect the line in both source-included and source-excluded spectra at consistent energy and flux, this points to the fact that the signal does not result from the point sources in the field; rather, it is extended in origin.

#### 4.3. Fit the Spectra with a Background Model

We have then fit the data plus background using two models at the same time for (1) the PIB described in Section 3.2 without folding it through the ARF and (2) the CXB model described in the previous two subsections folded through all of the response matrices. Since the PIB for the two data sets differs only in amplitude, in the PIB models the slopes ( $\Gamma_{\text{PIB},1}$ ,  $\Gamma_{\text{PIB},2}$ ) and the break energy ( $E_{\text{break}}$ ) parameters were tied while the normalizations (*norm*) were set as independent parameters. On top of that, we added the instrumental emission lines mentioned in Section 3.2 and the CXB component approximated with a power law absorbed with Galactic  $N_{\text{H}}$ , and we tested the presence of the 3.5 keV line. Overall, the model consists of 36 parameters, so given the number of data points here, any BIC or AIC test is meaningless (Schwarz 1978).

The fit results are reported in Figure 4 together with confidence contours obtained with MCMC. The line is detected with a significance of  $\sim 2.5\sigma$  with a lower, but still consistent, energy with respect to the background-subtracted case

( $I_{3.5} = 3.9^{+2.1}_{-2.5} \times 10^{-7}$  ph cm $^2$  s $^{-1}$  and  $E = 3.49^{+0.04}_{-0.03}$  keV). Also in this case, the probability distribution for  $I_{3.5}$  is skewed toward low values. However, in this fit we find an inconsistency between the CXB power-law normalizations  $I_{\text{PL},1}$  and  $I_{\text{PL},2}$  and those reported above. The reason is because, by fitting in the [2.4–7] keV energy range, the software does not have a means to disentangle the PIB and CXB power-law normalizations:  $I_{\text{PIB},1}$ ,  $I_{\text{PIB},2}$ ,  $I_{\text{PL},1}$ ,  $I_{\text{PL},2}$ , respectively. Indeed the  $\chi^2$  fit does not find a satisfactory value of the CXB spectral indices as most of the signal is spuriously attributed to the PIB. We decided to freeze the CXB spectral indices to  $\Gamma_{1,2} = 1.4$  (Cappelluti et al. 2017b). Most of the continuum parameters are highly covariant. For these reasons and because of the complexity of the model, we decided to rely on the background-subtracted scenarios that provide a more stable and model-independent result. For the same reason, we do not show the source-masked, background-modeled scenario.

#### 4.4. Safety Tests

Considering the marginal significance of the detection, we asked ourselves if the detected 3.5 keV line was a statistical fluctuation. As far as the 3.5 keV line is concerned, this is not a blind search since the energy of the line under investigation is known a priori. This means that the *look-elsewhere effect* in our measurement is not important or at least negligible. However, given the low signal-to-noise ratio of the detected signal, we tested the hypothesis that the observed line might be a statistical fluctuation in the background. In order to test this, we obtained 1000 random realizations of the best-fit spectrum without the 3.5 keV line via Monte Carlo integration. At the same time, we also drew 1000 random realizations of the stowed background spectrum. With these data sets in hand, we fitted every realization with the model including the 3.5 keV line and computed the cumulative distribution of the  $E_{3.5}$  and  $I_{3.5}$  fit results, and we found that, while the values of  $E_{3.5}$  are uniformly distributed between 3 and 4 keV ( $3\sigma$ ), the 3.5 keV line flux is always  $\ll 1.0 \times 10^{-6}$  ph cm $^2$  s $^{-1}$ , in agreement with our findings. However, since the background level is known with a  $\sim 2\%$  precision, we cannot at the moment exclude that systematic effects could indeed produce the observed line, but we point out that in the [3–4] keV band the overall spectrum is rather flat and the effective area is rather smooth. We also stress the fact that such a simulation is sensitive to statistical fluctuations only and not to systematic effects, which, in this case, can only be estimated.

### 5. Discussion

We discuss our findings in the context of earlier claims of detection of the 3.5 keV line by several other groups. The 3.5 keV line has been previously detected in the direction of the Perseus Cluster, in a stack of galaxy clusters, and, more recently, toward the Galactic center and in M31 by Bo14. Interestingly, the energy of the line is consistent with that detected in Perseus redshifted from  $z = 0.018$ . However, the recent nondetection by *Hitomi* (Hitomi Collaboration et al. 2017) rules out the highest flux detected by XMM-MOS in the direction of Perseus. Recently, Perez et al. (2017) made independent *NuSTAR* observations that are also relevant for testing the possibility of a 3.5 keV signal. They found a significant line flux at 3.5 keV. However, they also detected the line in observations where the Galactic center direction is

<sup>9</sup> We note that there is a substantial agreement with the B. Luo (2016, in preparation) CDFS 7 Ms catalog that became available after the submission of this paper.

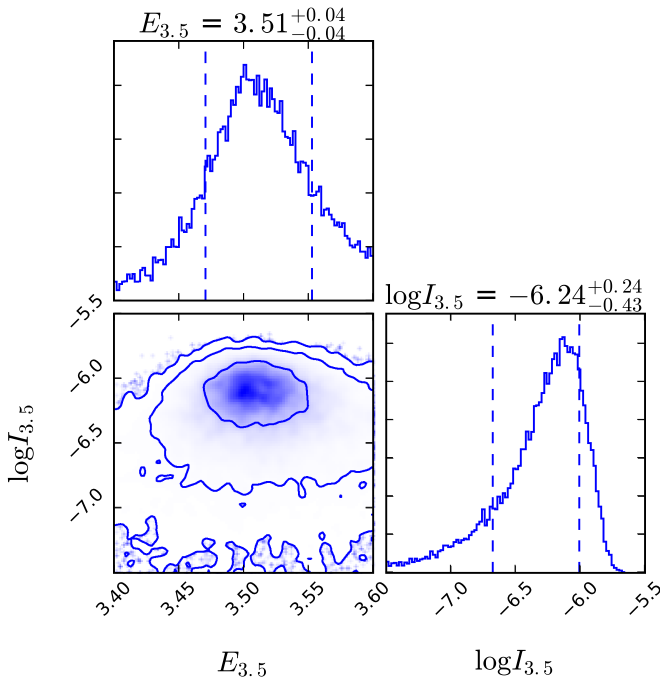


**Figure 2.** In blue color scale: the fit parameter confidence contours for the background-subtracted, source-masked case obtained with the MCMC analysis for the 3.5 keV-like parameters, intensity of line ( $\log(I_{3.5})$ ), and energy ( $E_{3.5}$ ). The contours levels are 1, 2, and  $\sigma$ , respectively.

blocked by Earth. As the nature of the 3.5 keV line (and another at 4.5 keV) in *NuSTAR* remains unknown, Perez et al. (2017) set deliberately conservative limits on the line fluxes that could be due to new signals.

In a recent paper, Neronov et al. (2016) reported an  $11\sigma$  detection of the 3.5 keV line in *NuSTAR* observations of the CCLS field and the CDFS. They observed the same areas of sky observed here, for a comparable exposure time, taking advantage of the fact that the *NuSTAR* detector, which was not shielded from indirect light, was able to effectively survey a total sky area of  $37.2 \text{ deg}^2$  viewed by a  $13' \times 13'$  detector area. This obviously provides increased leverage compared to telescopes sensitive to focused photons only. Interestingly, the line has been detected by Wik et al. (2014), but no hypothesis has been put forward for its origin. In fact, the line has been flagged as instrumental. *Chandra* and *NuSTAR* have the same collecting area at 3.5 keV, and the exposures used in these two papers are comparable. We can, therefore, directly compare the two results by transforming the observed fluxes into surface brightness ( $S$ ) under the assumption that the line flux is homogeneous over the  $37.5 \text{ deg}^2$ . However, for *NuSTAR* ( $S_{3.5,Nu}$ ), we have to take into effect the boosting factor introduced by the nonfocused component of the signal, so that

$$S_{3.5,Nu} = F_{3.5,Nu} / (\kappa(E) * 1.43 \times 10^{-5}), \quad (1)$$

where  $F_{3.5,Nu}$  is the flux of the line observed by *NuSTAR*, and  $\kappa(E)$  is the energy-dependent *boosting factor* for the *NuSTAR*-measured diffuse, indirect background. This takes into account the fact that the effective surveyed area is much larger than the area sensitive to focused photons.

At 3.5 keV, Neronov et al. (2016) report  $\kappa(E) \sim 7.5$ , and the FOV of the CdZnTe detector is  $1.43 \times 10^{-5} \text{ sr}$ , while ACIS-I's FOV is  $2.42 \times 10^{-5} \text{ sr}$ . Considering this, we find  $S_{3.5,Nu} = 0.093 \pm 0.023 \text{ ph cm}^{-2} \text{ s}^{-1} \text{ sr}^{-1}$  and

$S_{3.5,Nu} = 0.069 \pm 0.012 \text{ ph cm}^{-2} \text{ s}^{-1} \text{ sr}^{-1}$  with data taken in the shadow of the Earth and illuminated by the Sun, respectively, and  $S_{3.5,Ch} = 0.042 \pm 0.017 \text{ ph cm}^{-2} \text{ s}^{-1} \text{ sr}^{-1}$  with *Chandra*.

Our measurements are thus marginally consistent with *NuSTAR*'s by Neronov et al. (2016). Thus, it is possible that *Chandra* and *NuSTAR* are observing the same cosmic source of 3.5 keV photons. However, if the flux of the line is as measured by *NuSTAR*, we would have detected the line at at least  $5\sigma$ . However, it is worth noting that the calibration of the effective area of *NuSTAR* in that energy band is very unstable (as per information from the *NuSTAR* calibration team), and a 2% spike could be introduced by the fact that during the calibration the control points for the Crab fitting are at 3.3 and 3.68 keV; the Crab and hence the response have been corrected between these two energies with a straight line.

If the line is not an artifact, the *NuSTAR* detection is  $\sim 3$  times more significant because they collected 10 times more photons than *Chandra* did. Assuming a consistency between the measurements (even if marginal), given the differences in satellite orbits and detectors, means an instrumental or cosmic-ray origin for the signal is unlikely. The intensity of the line is the same both with the spacecraft illuminated by the Sun and in the shade of the Earth. Moreover, *Chandra* observations were taken over  $\sim 15$  years, while *NuSTAR* data were obtained in just the past 3 years, which argues against such transient causes such as the solar wind. However, the energy of the line is remarkably consistent with the two observations, taken with two different instrumental setups<sup>10</sup> under different geomagnetic conditions and at completely different times, which suggests an extrinsic source for the detected line. Hitomi Collaboration et al. (2017) speculated that the line might be a feature of CCD detectors, but this would not account for the *NuSTAR* detection with CdZnTe detectors.

Moreover, a recent analysis of the *Chandra* PIB by Bartalucci et al. (2014) did not find any residuals or emission lines between 3 and 5.8 keV. While we cannot exclude further unaccounted for and as yet unknown effects introduced by the mirrors or the CCD, based on this concordance, the instrumental origin seems to be less likely given multiple detections in the data taken with different instruments and under different conditions. A further source of concern is the contamination of the ACIS optical blocking filter by a deposit of hydrocarbons. This effect has been known for many years and is well understood. Moreover, while this effect is dramatic in the soft bands, it is small above 3 keV, and we consider it negligible. We also investigated the possibility that tin whiskers (crystalline structures of tin growing when tin coatings are used as a finish) might be implicated, since  $\text{Sn}_{50}$  presents energetic transitions in L shells around 3.5 keV. However, consultation with the *Chandra* engineering team suggests that the amount of tin is relatively small, but we could not estimate its contribution to our observations. Still, further calibrations and deeper studies of the spectral dependence of the instrument response are needed and will be important for firmly establishing the reality (or not) of this emission feature. In particular, we would recommend deeper integrations of the stowed background.

With this analysis, we can affirm that, unless the *Chandra* effective area calibration has problems at 3.5 keV that remain undetected despite substantial attention to this energy, we can exclude an instrumental origin for the line. We now proceed to

<sup>10</sup> ACIS-I is a silicon CCD, while the imagers of *NuSTAR* are two cadmium-zinc-telluride detectors.

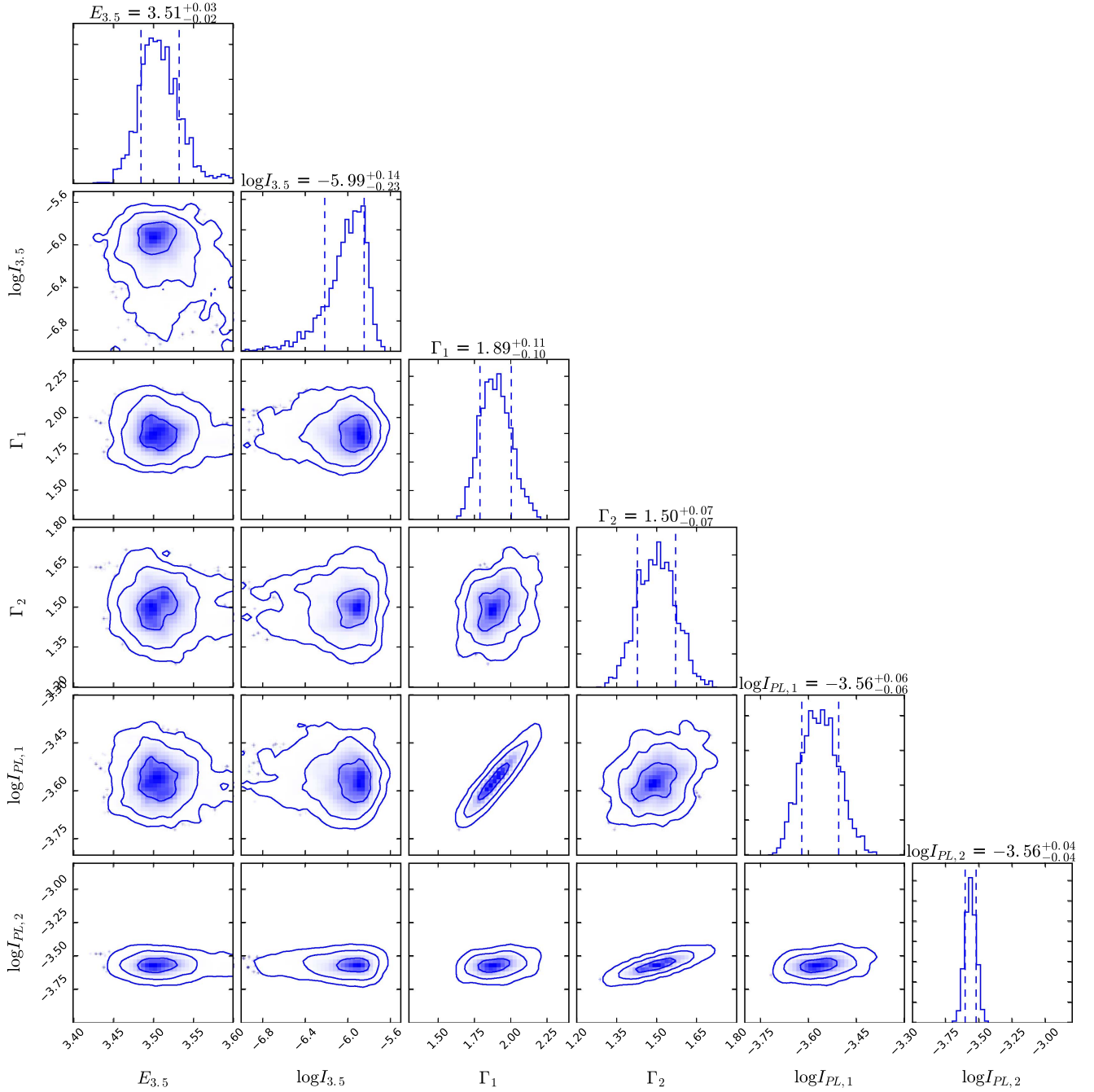


**Figure 3.** In blue color scale: the fit parameter confidence contours for the background-subtracted full detector case obtained with the MCMC analysis for the relevant parameters. The contour levels are 1, 2, and  $\sigma$ , respectively. For every parameter, we plot the marginal probability distribution histogram on top of every column, where we show the  $1\sigma$  intervals with dashed lines. We also report the best-fit values and the  $1\sigma$  confidence level. From top to bottom the parameters are energy ( $E_{3.5}$ ) and logarithm of the intensity of the 3.5 keV line ( $\log(I_{3.5})$ ), the CXB spectral index in the CDFS  $\Gamma_1$ , the spectral index in the CCLS  $\Gamma_2$ , and the logarithm of the normalization of the continuum in the CDFS ( $\log(I_{PL,1})$ ) and in the CCLS ( $\log(I_{PL,2})$ ).

discuss possible physical mechanisms that can produce an emission line at 3.5 keV.

### 5.1. The Iron Line Background

Regardless of the nature of the search, we know that when observing the CXB, we are witnessing the accretion history onto supermassive black holes across cosmic time. There is evidence that a large fraction of the accretion in the universe occurs in an obscured phase (see, e.g., Treister & Urry 2005; Gilli et al. 2007). One characteristic feature of such a phase of accretion is a strong Fe  $K_\alpha$  6.4 keV emission line. Such an

emission line has been significantly detected in stacked spectra of AGNs divided into redshift bins (see, e.g., Brusa et al. 2005; Chaudhary et al. 2010; Falocco et al. 2013), with a very intense contribution from sources at  $z \sim 0.7\text{--}0.9$  (i.e., Fe  $K_\alpha$  redshifted to 3.5 keV), where the cosmic AGN activity was near its peak. However, the CXB spectrum contains the emission from AGNs from all redshifts, and its intensity is modulated by the redshift distribution of the sources and their luminosity distance. Gilli et al. (1998, 1999) modeled this emission and found that the redshift distribution smooths this signal into an “inverse edge”-shaped feature between 2 and 4 keV. The intensity of such a



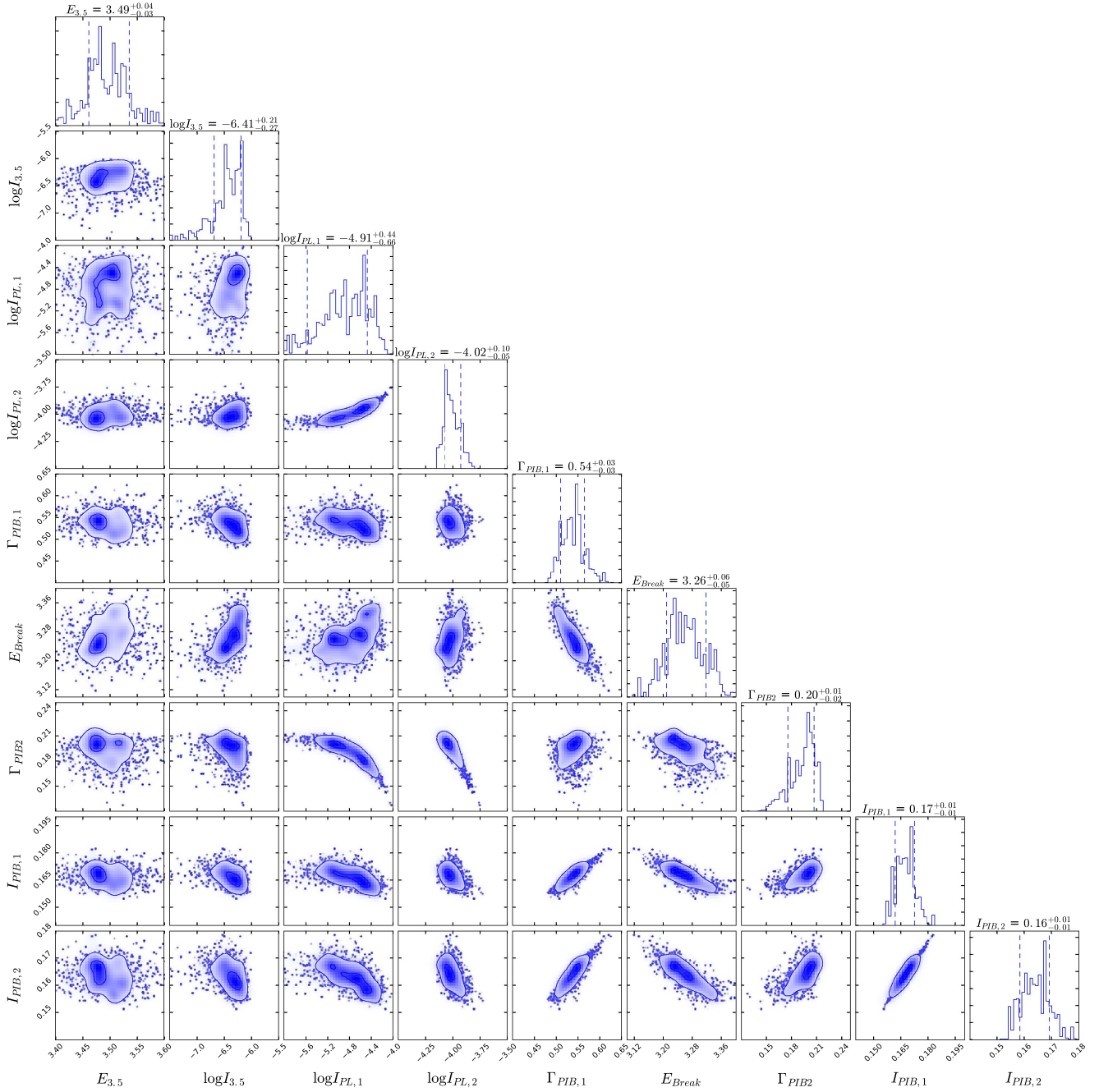


**Figure 4.** In blue color scale: the fit parameter confidence contours for the background-modeled full detector case obtained with the MCMC analysis for the relevant parameters. The contours levels are 1, 2, and 3 $\sigma$ , respectively. For every parameter, we plot the marginal probability distribution histogram on top of every column, where we show the 1 $\sigma$  intervals with dashed lines. We also report the best-fit values and the 1 $\sigma$  confidence level. From top to bottom, the parameters are energy ( $E_{3.5}$ ) and logarithm of the intensity of the 3.5 keV line ( $\log(I_{3.5})$ ), the CXB logarithm of the normalization of the continuum in the CDFS ( $\log(I_{PL,1})$ ) and in the CCLS ( $\log(I_{PL,2})$ ), the PIB spectral index in the CDFS ( $\Gamma_{PIB,1}$ ), the break energy ( $E_{Break}$ ), the PIB spectral index in the CCLS ( $\Gamma_{PIB,2}$ ), the break energy  $E_{Break}$ , and the PIB logarithm of the normalization of the continuum in the CDFS ( $I_{PIB,1}$ ) and in the CCLS ( $I_{PIB,2}$ ).

feature is a few percent above the continuum at about 3.5 keV. However, since the redshift distribution of the resolved sources is not smooth but shows spikes due to the presence of a large-scale structure, the feature appears near or at the energy of such spikes. Both COSMOS and the CDFS do not show prominent spikes in their AGN redshift distribution around  $z \sim 0.8$  (Luo et al. 2017; Marchesi et al. 2016). Given this, together with the lack an “inverse edge” feature in the spectrum, we can safely state that this scenario is unlikely and can be excluded.

### 5.2. 3.5 keV Line from SXVI Charge Exchange

Gu et al. (2015) suggested that the 3.5 keV line could be attributed to charge exchange (CX) between neutral hydrogen and bare sulfur ions. This collision leads to the full Lyman series of transitions in S XVI, with a strong Ly $_{\alpha}$  at 2.62 keV and, crucially, enhanced high- $n$  transitions around the Ly $_{\eta}$  and Ly $_{\theta}$  (i.e.,  $n = 8 \rightarrow 1$ ,  $9 \rightarrow 1$ ) transition. These enhanced high- $n$  lines are the indicator of CX, driven by capture into the high- $n$  shells that does not occur during electron-impact collisional



**Table 4**  
Predicted S XVI Charge-exchange Transition Lines

Transition	Energy keV	$I_E/I_{2.62}$ $10^{-6} \text{ ph cm}^{-2}$	$I(E)$
2 $\rightarrow$ 1	2.621	1.0	<2.98
3 $\rightarrow$ 1	3.106	0.142	<1.45
4 $\rightarrow$ 1	3.276	0.050	<0.64
5 $\rightarrow$ 1	3.354	0.025	<0.51
6 $\rightarrow$ 1	3.397	0.016	<0.64
7 $\rightarrow$ 1	3.423	0.011	1.02 <sup>a</sup>
8 $\rightarrow$ 1	3.434	0.120	1.02 <sup>a</sup>
9 $\rightarrow$ 1	3.451	0.074	1.02 <sup>a</sup>

**Note.**

<sup>a</sup> Assuming the detected 3.5 keV flux.

excitation. Significantly, for this work, these lines lie in the 3.4–3.45 keV energy band. The exact ratios of the lines in the Lyman series depend on the exact  $n$  and  $l$  shell into which the electron is captured. In particular, the  $l$  shell is very sensitive to the collision energy, although calculations of the relative cross section are sparse and highly likely to disagree. We have used data from the AtomDB Charge Exchange (ACX) model (Smith et al. 2012) to obtain the line energies and relative intensities shown in Table 4. In this case, we have used ACX model 8, which is the separable  $l$  distribution and the weighted  $n$  distribution (described in Smith et al. 2012). This corresponds to a relatively low center-of-mass velocity ( $\lesssim 1000 \text{ km s}^{-1}$ ), which is appropriate for a thermal plasma such as this one, but the results do not change significantly if other distributions are used instead.

In all of these observed scenarios, the intensity of the Ly $\alpha$  line is 5 times that of the 3.4–3.45 keV line complex. We do not detect a line with an energy consistent with 2.62 keV, although we can determine an upper limit for its intensity at  $<2.98 \times 10^{-6} \text{ ph cm}^{-2}$ . By assuming that all of the  $\sim 3.5$  keV emission is produced by S XVII CX, and considering the energy resolution of *Chandra* (of the order of 150 eV) and *NuSTAR* (400 eV), we test the hypothesis of Gu et al. (2015) and Shah et al. (2016) that we are seeing a blend of all the possible transitions around 3.4–3.45 keV. Although the energy of the line detected here is clearly in tension with the predictions for S XVII CX, the discrepancy just might be a consequence of the energy resolution of the instrument.

From the values in Table 4, we expect a line ratio  $I_{3.45}/I_{2.62}$  of  $\leq 0.2$ , where  $I_{3.45}$  is the intensity of the 3.45 keV line system. In our case, the ratio is  $>0.34$ , which rules out CX together with a discrepant energy. In addition, any signal at 2.62 keV, which we can interpret here as the  $n = 2 \rightarrow 1$  S XVII transition, can also be attributed to the daughter lines of the instrumental feature at 2.1 keV. Any such contribution would, in effect, raise the observed ratio, making CX less likely. In addition, the CX process should also produce a significant Ly $\beta$  line at 3.106 keV: we do not observe any such line, but we can only place an upper limit (see Table 4). Another possible CX transition that occurs near 3.5 keV is the Ar XVIII  $n = 2 \rightarrow 1$  transition at 3.32 keV, where we do not detect any line nor do we see any evidence of higher  $n$  shell transitions from this ion. According to these measurements and atomic calculations, we can rule out that the totality of the 3.5 keV line flux measured here is produced by CX.

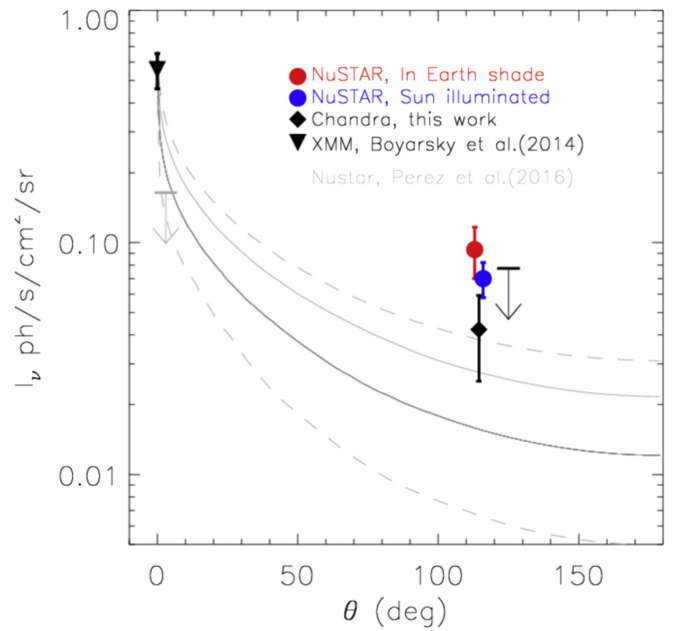


**Figure 5.** The  $1\sigma$  (solid line) and  $2\sigma$  (dashed line) limits on the expected 3.5 keV line flux as a function of the angular distance from the GC by assuming an NFW profile with parameters from Nesti & Salucci (2013) and DM flux at  $\theta = 0$  from Boyarsky et al. (2014). The profile is compared with our measurements from the deep fields (black solid circles) and with the *NuSTAR* results (red and blue solid circles). The downward-pointing black arrow represents the  $3\sigma$  limit derived from simulations.

### 5.3. 3.5 keV Line from Dark Matter Decay

One of the possible interpretations of the detection of the 3.5 keV emission line is the decay of sterile neutrinos into a neutrino and an X-ray photon (Pal & Wolfenstein 1982). If the emission originates from dark matter decay, then the line flux would be proportional to the amount of matter along the line of sight over the field of view. In the present case, we would expect the Milky Way dark matter halo to dominate the local signal (Riemer-Sørensen et al. 2006). With this data set, we sample the dark matter halo distribution along the line of sight, and, therefore, the emission seen should scale with the amount of mass sampled.

Boyarsky et al. (2014), detected the 3.5 keV line in the direction of the GC. The observed fields presented here lie at an aperture angle  $\theta$  with respect to the galaxy center (GC). If our detected signal comes from dark matter (DM) decay within the Milky Way (MW) halo, then its intensity should be

$$I_{\text{DM}}(\theta) = I_{\text{DM,GC}} \frac{\int \rho_{\text{DM}}[r(l, 0^\circ)] dl d\Omega}{\int \rho_{\text{DM}}[r(l, \theta)] dl d\Omega}, \quad (2)$$

where  $I_{\text{DM}}(\theta)$  is the DM decay signal at aperture angle  $\theta$  from the GC,  $I_{\text{DM,GC}}$  is the DM decay signal from the GC ( $\theta = 0$ ),  $\rho(r)$  is the DM density profile,  $l$  is the distance along the line of sight, and  $r$  and  $\theta$  are the physical and angular distance from the center of the galaxy, respectively. The three quantities are related via

$$r(l, \theta) = \sqrt{l^2 + d^2 - 2ld \cos(\theta)}, \quad (3)$$

where  $d$  is the distance of the earth from the GC. We note that the distance and MW DM profile parameters and shape are still highly debated (Bland-Hawthorn & Gerhard 2016).

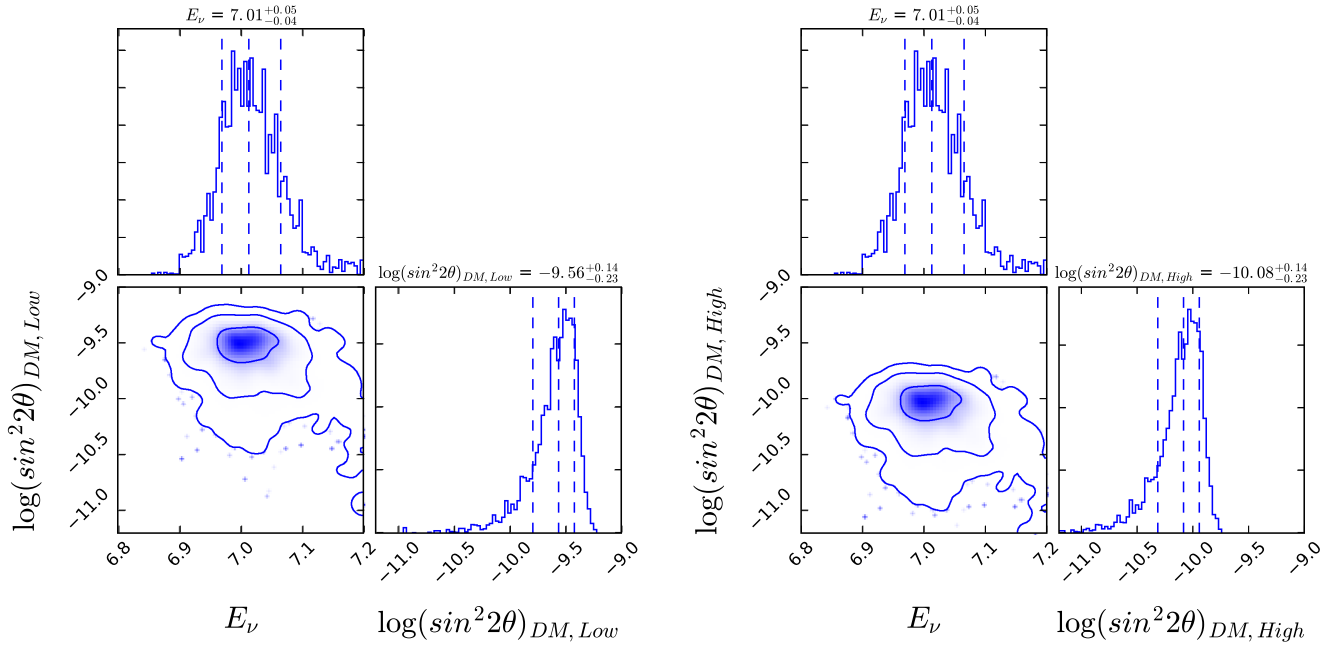


**Figure 6.** Confidence contours derived for sterile neutrino parameters  $E_\nu$  and  $\sin^2 2\theta$  from our MCMC for the cases of low and high integrated surface mass density of DM ( $\Sigma_{\text{DM}}$ ), left and right, respectively.

Assume that all of the intervening dark matter is associated with a cold component that can be modeled with a Navarro–Frenk–White (NFW) profile (Navarro et al. 1997) given by

$$\rho_{\text{DM}} = \frac{\rho^*}{x(1+x)^2}, \quad (4)$$

where  $x = r/r_{\text{H}}$ ; here we adopt the parameters measured by Nesti & Salucci (2013) and therefore use  $d = 8.02 \pm 0.2$  kpc,  $r_{\text{H}} = 16.1^{+12.2}_{-5.6}$ ,  $\rho^* = 13.8^{+20.7}_{-6.6} \times 10^6 M_\odot \text{ kpc}^{-3}$ , and  $I_{\text{DM, GC}} = 0.63 \pm 0.11 \text{ ph s}^{-1} \text{ cm}^{-2} \text{ sr}^{-1}$ . Using Equation (2), we calculated, with Monte Carlo integration, the  $1\sigma$  and  $2\sigma$  confidence levels of the flux from DM decay along the line of sight as a function of the angular distance from the GC. This is shown in Figure 5, wherein we overplot our measurement and the *NuSTAR* measurement. The two fields investigated here are basically at the same angular distance from the GC of  $\theta \sim 115^\circ$ . Remarkably, our measurements are consistent at the  $1\sigma$  level with such a profile. This means the ratio of fluxes at  $\theta = 115$  and  $\theta = 0$  is consistent with the NFW DM decay model. We also point out that we assumed that Sgr A\* coincides with the center of the MW DM halo.

In terms of constraints on the number of neutrino species (allowing one additional species of a sterile neutrino along with the three other usual flavors), Planck Collaboration et al. (2016) report that with the CMB temperature data alone it is difficult to constrain  $N_{\text{eff}}$ , and data from Planck alone do not rule out  $N_{\text{eff}} = 4$ . At the 95% C.L. combining Planck + *WMAP* + high  $l$  experiments, they obtain  $N_{\text{eff}} = 3.36^{+0.68}_{-0.64}$ . The Planck collaboration has only investigated an electronvolt-mass sterile neutrino as a potential additional species. So other than saying that  $N_{\text{eff}} = 4$  is permitted, we find there are no concrete CMB constraints on kiloelectronvolt sterile neutrinos.

Performing the line integral through the halo of the Milky Way taking into account the FOV and given that all three deep fields included in this analysis are at roughly  $115^\circ$ , we compute the surface mass density along the line of sight. Similar to our

assumption adopted above, the MW halo is once again modeled with an NFW profile, and the current best-fit parameters are adopted from Nesti & Salucci (2013). Using the formulation developed in Abazajian et al. (2007), we use the measured flux in the line to constrain the mixing angle  $\sin^2 2\theta$ . Although we use the integrated surface mass density of dark matter in the Milky Way halo integrated out to the virial radius, the dominant contribution comes from the inner region—from within a few scale radii—of the density profile, due to the shape of the NFW profile. Using the higher bound and the lower bound estimates for the total mass of the Milky Way, we obtain the following values for  $\Sigma$  of the integrated surface mass density of DM:

$$\begin{aligned} \Sigma_{\text{DM, High}} &= 0.0362 \text{ gm cm}^{-2}; \\ \Sigma_{\text{DM, Low}} &= 0.0109 \text{ gm cm}^{-2}. \end{aligned} \quad (5)$$

Using these values and the equation

$$\begin{aligned} \sin^2 2\theta \times \left( \frac{m_\nu}{1 \text{ keV}} \right)^4 \times \frac{\Sigma_{\text{DM}}}{\text{gm cm}^{-2}} \\ = \left( \frac{I_\nu}{1.45 \times 10^{-4}} \right) \text{ photons cm}^{-2} \text{ s}^{-1} \text{ arcsec}^{-2}, \end{aligned} \quad (6)$$

we obtain that  $\sin^2 2\theta_{\text{DM, High}} = 0.83^{+0.34}_{-0.31} \times 10^{-10}$  and  $\sin^2 2\theta_{\text{DM, Low}} = 2.75^{+1.13}_{-1.04} \times 10^{-10}$ . The confidence contours for the sterile neutrino parameters are summarized in Figure 6. Furthermore, we can now estimate the lifetime  $\tau$  for this sterile neutrino species, using Equation (2) of Boyarsky et al. (2015):

$$\tau_{\text{DM}} = 7.2 \times 10^{29} \text{ s} \left( \frac{10^{-8}}{\sin^2 2\theta} \right) \left( \frac{1 \text{ keV}}{m_\nu} \right)^5, \quad (7)$$

and we find that it is  $\tau_{\text{DM, High}} = 5.16^{+3.56}_{-1.42} \times 10^{27} \text{ s}$  and  $\tau_{\text{DM, Low}} = 1.55^{+1.06}_{-0.43} \times 10^{27} \text{ s}$ , respectively. These mixing angle estimates are in very good agreement with Figures 13 and 14 of Bul14a. They

can also be overplotted and seen clearly to be consistent with Figure 3 of Iakubovskiy et al. (2015).

However, despite concordance with parameters extracted from other observational constraints obtained from X-ray data of stacked galaxy clusters and the Galactic center, due to the significance of our detection only at the  $\sim 3\sigma$  level, we cannot conclusively claim that this observed 3.51 keV line originates from decaying dark matter. It would require a nondetection with at least 100 Ms of *Chandra* observations to rule out this hypothesis.

## 6. Summary


In this paper, we perform a systematic search for an emission feature at  $\sim 3.5$  keV in the spectrum of the CXB with extremely deep *Chandra* integration time. We find evidence of a feature with a significance of  $2.5\text{--}3\sigma$ , depending on the statistical treatment of the data. The evaluation of the significance of the line is further complicated by the complexity of the model and the weak nature of the signal. In particular, estimating the relation between  $\Delta\chi^2$  and  $P$  is complicated because of model misspecification. Additionally, regardless of the significance of the feature, we are able to place a  $3\sigma$  upper limit on the line intensity. Examining the sources of a possible origin for this feature, we conclude that the line does not have a clear known instrumental origin. The intensity and the energy of the line are consistent with earlier measurements that were interpreted as decay of an  $\sim 7$  keV sterile neutrino, and the decay rate found here is in remarkable agreement with previous work. We can interpret the signal as DM decay along the line of sight in the Milky Way halo.

We also investigate the scenario wherein the 3.5 keV flux is produced by charge exchange between neutral hydrogen and bare sulfur ions. We conclude that all of the 3.5 keV flux cannot be produced by charge exchange. We also discuss a scenario in which the line could be produced by a blend of redshifted iron lines from AGNs by large-scale structures that spike at  $z \sim 0.8$ . This interpretation would be consistent with predictions for the iron line background but not (1) with cluster measurements (Bul14a) and (2) with the lack of prominent spikes in the redshift distribution at that redshift. We can conclude that charge exchange and the iron line background together cannot produce more than  $1.85 \times 10^{-6} \text{ ph cm}^{-2} \text{ s}^{-1}$  at 3.5 keV. So far, the 3.5 keV line is the only feature detected from four independent instruments that is interpretable as DM decay (*Chandra*, *XMM-Newton*, *Suzaku*, and *NuSTAR*) with more than one  $>5\sigma$  detection in a variety of DM-dominated objects. Given the amount of data available in the archives, an intensive data-mining exercise of X-ray spectra is an extremely cost- and time-effective method to rule out or confirm the contribution of sterile neutrinos to DM. The nature of dark matter is a key unsolved problem in cosmology, and at the moment we seem to be at an impasse in terms of both direct and indirect detection experiments (see, e.g., Ackermann et al. 2015; IceCube Collaboration et al. 2017). Therefore, further and even more careful analysis of existing X-ray observations is warranted and crucial. In the future, X-ray calorimeters on board *X-ray Astronomy Recovery Mission*, *Athena*, or the Micro-X sounding rocket (Figueroa-Feliciano et al. 2015) will greatly improve our understanding of the origin of the 3.5 keV feature given their capability for high-precision spectroscopy.

N.C. acknowledges the Yale University YCAA Prize fellowship postdoctoral program. P.N. acknowledges a Theoretical and

Computational Astrophysics Network grant with award number 1332858 from the National Science Foundation and thanks the Aspen Center for Physics, which is supported by the National Science Foundation grant PHY-1066293, where this work was done in part. E.B. acknowledges support from NASA grant NNX13AE77G.

## ORCID iDs

Nico Cappelluti  <https://orcid.org/0000-0002-1697-186X>

Adam Foster  <https://orcid.org/0000-0003-3462-8886>

Priyamvada Natarajan  <https://orcid.org/0000-0002-5554-8896>

Randall K. Smith  <https://orcid.org/0000-0003-4284-4167>

## References

- Abazajian, K., Fuller, G. M., & Tucker, W. H. 2001, *ApJ*, **562**, 593
- Abazajian, K. N., Markevitch, M., Koushiappas, S. M., & Hickox, R. C. 2007, *PhRvD*, **75**, 063511
- Ackermann, M., Ajello, M., Albert, A., et al. 2015, *PhRvD*, **91**, 122002
- Anderson, M. E., Churazov, E., & Bregman, J. N. 2015, *MNRAS*, **452**, 3905
- Arnaud, K. A. 1996, in ASP Conf. Ser. 101, *Astronomical Data Analysis Software and Systems V*, ed. G. H. Jacoby & J. Barnes (San Francisco, CA: ASP), 17
- Bartalucci, I., Mazzotta, P., Bourdin, H., & Vikhlinin, A. 2014, *A&A*, **566**, A25
- Bland-Hawthorn, J., & Gerhard, O. 2016, *ARA&A*, **54**, 529
- Boyersky, A., Franse, J., Iakubovskiy, D., & Ruchayskiy, O. 2015, *PhRvL*, **115**, 161301
- Boyersky, A., Neronov, A., Ruchayskiy, O., Shaposhnikov, M., & Tkachev, I. 2006, *PhRvL*, **97**, 261302
- Boyersky, A., Ruchayskiy, O., Iakubovskiy, D., & Franse, J. 2014, *PhRvL*, **113**, 251301
- Brusa, M., Gilli, R., & Comastri, A. 2005, *ApJL*, **621**, L5
- Bulbul, E., Markevitch, M., Foster, A., et al. 2014, *ApJ*, **789**, 13
- Bulbul, E., Markevitch, M., Foster, A., et al. 2016, *ApJ*, **831**, 55
- Capak, P., Aussel, H., Ajiki, M., et al. 2007a, *ApJS*, **172**, 99
- Cappelluti, N., Arendt, R., Kashlinsky, A., et al. 2017b, *ApJL*, **847**, L11
- Cappelluti, N., Comastri, A., Fontana, A., et al. 2016, *ApJ*, **823**, 95
- Cappelluti, N., Li, Y., Ricarte, A., et al. 2017a, *ApJ*, **837**, 19
- Chaudhary, P., Brusa, M., Hasinger, G., Merloni, A., & Comastri, A. 2010, *A&A*, **518**, A58
- Civano, F., Marchesi, S., Comastri, A., et al. 2016, *ApJ*, **819**, 62
- Conlon, J. P., & Day, F. V. 2014, *JCAP*, **11**, 033
- Dickey, J. M., & Lockman, F. J. 1990, *ARA&A*, **28**, 215
- Dodelson, S., & Widrow, L. M. 1994, *PhRvL*, **72**, 17
- Dolgov, A. D., & Hansen, S. H. 2002, *APh*, **16**, 339
- Elvis, M., Civano, F., Vignali, C., et al. 2009, *ApJS*, **184**, 158
- Falocco, S., Carrera, F. J., Corral, A., et al. 2013, *A&A*, **555**, A79
- Figueroa-Feliciano, E., Anderson, A. J., Castro, D., et al. 2015, *ApJ*, **814**, 82
- Foster, A. R., Ji, L., Smith, R. K., & Brickhouse, N. S. 2012, *ApJ*, **756**, 128
- Franse, J., Bulbul, E., Foster, A., et al. 2016, *ApJ*, **829**, 124
- Giacconi, R., Zirm, A., Wang, J., et al. 2002, *ApJS*, **139**, 369
- Gilli, R., Comastri, A., Brunetti, G., & Setti, G. 1998, *AN*, **319**, 65
- Gilli, R., Comastri, A., Brunetti, G., & Setti, G. 1999, *NewA*, **4**, 45
- Gilli, R., Comastri, A., & Hasinger, G. 2007, *A&A*, **463**, 79
- Gu, L., Kaastra, J., Raassen, A. J. J., et al. 2015, *A&A*, **584**, L11
- Hickox, R. C., & Markevitch, M. 2006, *ApJ*, **645**, 95
- Hickox, R. C., & Markevitch, M. 2007, *ApJL*, **661**, L117
- Hitomi Collaboration, Aharonian, F. A., Akamatsu, H., et al. 2017, *ApJL*, **837**, L15
- Horiuchi, S., Bozek, B., Abazajian, K. N., et al. 2016, *MNRAS*, **456**, 4346
- Iakubovskiy, D., Bulbul, E., Foster, A. R., Savchenko, D., & Sadova, V. 2015, *arXiv:1508.05186*
- IceCube Collaboration, Aartsen, M. G., Ackermann, M., et al. 2017, *EPJC*, **77**, 146
- Jeltema, T., & Profumo, S. 2015, *MNRAS*, **450**, 2143
- Luo, B., Bauer, F. E., Brandt, W. N., et al. 2008, *ApJS*, **179**, 19
- Luo, B., Brandt, W. N., Xue, Y. Q., et al. 2017, *ApJ*, **228**, 2
- Marchesi, S., Civano, F., Elvis, M., et al. 2016, *ApJ*, **817**, 34
- Moretti, A., Vattakunnel, S., Tozzi, P., et al. 2012, *A&A*, **548**, A87



- Navarro, J. F., Frenk, C. S., & White, S. D. M. 1997, [ApJ](#), **490**, 493
- Neronov, A., Malyshev, D., & Eckert, D. 2016, [PhRvD](#), **94**, 123504
- Nesti, F., & Salucci, P. 2013, [JCAP](#), **7**, 016
- Pal, P. B., & Wolfenstein, L. 1982, [PhRvD](#), **25**, 766
- Perez, K., Ng, K. C. Y., Beacom, J. F., et al. 2017, [PhRvD](#), **95**, 123002
- Planck Collaboration, Ade, P. A. R., Aghanim, N., et al. 2016, [A&A](#), **594**, A16
- Protassov, R., van Dyk, D. A., Connors, A., Kashyap, V. L., & Siemiginowska, A. 2002, [ApJ](#), **571**, 545
- Riemer-Sørensen, S., Hansen, S. H., & Pedersen, K. 2006, [ApJL](#), **644**, L33
- Rubin, V. C., & Ford, W. K., Jr. 1970, [ApJ](#), **159**, 379
- Ruchayskiy, O., Boyarsky, A., Iakubovskyi, D., et al. 2016, [MNRAS](#), **460**, 1390
- Schwarz, G. 1978, [AnSta](#), **6**, 461
- Scoville, N., Aussel, H., Brusa, M., et al. 2007, [ApJS](#), **172**, 1
- Shah, C., Dobrodey, S., Bernitt, S., et al. 2016, [ApJ](#), **833**, 52
- Smith, R. K., Brickhouse, N. S., Liedahl, D. A., & Raymond, J. C. 2001, [ApJL](#), **556**, L91
- Smith, R. K., Foster, A. R., & Brickhouse, N. S. 2012, [AN](#), **333**, 301
- Spanos, A. 2010, [Journal of Econometrics](#), 158, 204
- Treister, E., & Urry, C. M. 2005, [ApJ](#), **630**, 115
- Urban, O., Werner, N., Allen, S. W., et al. 2015, [MNRAS](#), **451**, 2447
- Vikhlinin, A., Burenin, R. A., Ebeling, H., et al. 2009, [ApJ](#), **692**, 1033
- Wik, D. R., Hornstrup, A., Molendi, S., et al. 2014, [ApJ](#), **792**, 48
- Xue, Y. Q., Luo, B., Brandt, W. N., et al. 2011, [ApJS](#), **195**, 10